Evaluating the effects of burn severity and precipitation on post-fire watershed responses using distributed hydrologic models

Zhi Li[1], Bing Li[1], Peishi Jiang[1], Glenn E. Hammond[1], Pin Shuai[2], Faria T. Zahura[1], Ethan T. Coon[3], Xingyuan Chen[1]

[1]Atmospheric, Climate and Earth Sciences Division, Pacific Northwest National Laboratory, Richland, WA, United States
[2]Utah Water Research Laboratory, Utah State University, Logan, UT, United States
[3]Climate Change Science Institute & Environmental Sciences Division, Oak Ridge National Laboratory, Oak Ridge, TN, United States

Key Points:

- The fire-caused soil water repellency is quantified using burn severity products and is incorporated into the integrated hydrologic model
- High burn severity wildfires cause increased peak flow discharges and decreased infiltration after the first post-fire precipitation event
- Higher post-fire precipitation events induce larger increase of the peak flow discharges due to the soil water repellency effect

Corresponding author: Xingyuan Chen, (xingyuan.chen@pnnl.gov)

Abstract

Wildfires can induce an abundance of vegetation and soil changes that may trigger higher surface runoff and soil erosion, affecting the water cycling within these ecosystems. In this study, we employed the Advanced Terrestrial Simulator (ATS), an integrated and fully distributed hydrologic model at watershed scale to investigate post-fire hydrologic responses in a few selected watersheds with varying burn severity in the Pacific Northwest region of the United States. The model couples surface overland flow, subsurface flow, and canopy biophysical processes. We developed a new fire module in ATS to account for the fire-caused hydrophobicity in the topsoil. Modeling results show that the watershed-averaged evapotranspiration is reduced after high burn severity wildfires. Post-fire peak flows are increased by 21-34% in the three study watersheds burned with medium to high severity due to the fire-caused soil water repellency (SWR). However, the watershed impacted by a low severity fire only witnessed a 2% surge in post-fire peak flow. Furthermore, the high severity fire resulted in a mean reduction of 38% in the infiltration rate within fire-impacted watershed during the first post-fire wet season. Hypothetical numerical experiments with a range of precipitation regimes after a high severity fire reveal the post-fire peak flows can be escalated by 1-34% due to the SWR effect triggered by the fire. This study implies the importance of applying fully distributed hydrologic models in quantifying the disturbance-feedback loop to account for the complexity brought by spatial heterogeneity.

Plain Language Summary

The increasing number of wildfires in the Pacific Northwest are changing the local soil and landscapes, potentially leading to increased water runoff, more soil erosion, and altered water quality. Despite attempts to study this, a thorough understanding of the long-term and large-scale impacts is lacking. We used a comprehensive computer model, including a new element for fire-induced soil water repellency, on freely available data to study watersheds affected by wildfires. Most showed an increase in peak water flow due to the fire's effect on soil, except one watershed with a less severe fire. Another watershed saw a decrease in water entering the soil after the fire. Our research compares water systems before and after fires, helping to further studies on the affects of fire on nutrients and sediment movement.

1 Introduction

In recent years, wildfires have caused "cascading hazards" across the globe (Hallema et al., 2018; Wagenbrenner et al., 2021; Kemter et al., 2021; Robinne et al., 2021). The Pacific Northwest of the United States represents a primary locus of wildfire activity and is denoted as one of the most significantly impacted regions globally. Wildfires in the Pacific Northwest region have been and continue to escalate in both frequency and severity (Li et al., 2021; Abatzoglou, Battisti, et al., 2021). As a significant disturbance to the ecosystem, wildfires are directly responsible for the spatiotemporal redistribution of carbon and nitrogen nutrients (Roebuck Jr et al., 2022), deteriorated water and air qualities (Wine & Cadol, 2016; Moisseeva & Stull, 2021; Wilmot et al., 2022; Paul et al., 2022), debris flow hazards (Rengers et al., 2016; DiBiase & Lamb, 2020), water supply risks (Wieting et al., 2017), and extreme flooding (Moody & Ebel, 2012). Many of the previously mentioned post-fire hazard cascades are the consequences of indirect fire effects that involve other spatiotemporal non-fire factors, combined with a direct fire effect caused by combustion—the substantial change on the soil physical properties, leading to the occurrence of soil water repellency (SWR) (DeBano, 2000a, 2000b; Garcia-Chevesich et al., 2010; Moody, 2012; Ebel et al., 2012; Murphy et al., 2015; Ebel et al., 2016; Murphy et al., 2018; Agbeshie et al., 2022). In SWR, the hydrophobic layer that forms in the soil as a consequence of fire exhibits reduced permeability compared to its pre-fire state. As water is the main

medium of transport processes in the ecosystem, the repartitioning of water between the surface and subsurface due to the SWR effect can be substantial at large scales and further break the pre-fire dynamic patterns of transport processes post-fire.

The consideration of SWR in various numerical modeling efforts has been limited. Those efforts have been undertaken to investigate the hydrologic effects of wildfires across diverse spatial and temporal scales, ranging from 1D soil column simulations to 3D integrated watershed analyses (Cydzik & Hogue, 2009; Chen et al., 2013; Kinoshita et al., 2014; Zema et al., 2020; Maina & Siirila-Woodburn, 2020; Wilder et al., 2021; Wampler et al., 2023). Ebel et al. (2023) summarized recent work evaluating the post-wildfire hydrologic response using physically based numerical models and identified key future research directions. One of the key future directions pointed out by Ebel et al. (2023) is to *include vadose zone and saturated zone processes to better capture subsurface streamflow generation*. To represent the fire impact on watershed hydrology, Maina and Siirila-Woodburn (2020) replaced the pre-fire land cover types in the burn scar areas with barren soil, but neglected the SWR effect on watershed hydrology. There are limited studies that employ high-resolution integrated hydrology specifically designed to account for the long-term effects of wildfires on a watershed-scale.

To address these gaps, in this study we employed a fully distributed hydrologic model known as the Advanced Terrestrial Simulator (ATS), which integrates surface overland flow, subsurface flow, and land surface processes including snow melt and canopy interception. As pointed out by Cydzik and Hogue (2009) and Chen et al. (2013), physically-based approaches are encouraged to be applied for more accurate predictions of fire-impacted hydrology. To incorporate SWR into the model, we developed a novel fire module within the ATS high-performance computing framework. We set up models with higher temporal resolution (hours) and spatial resolution (tens of meters) to capture relevant fine-scale temporal variations and microtopographic features. The model inputs encompass extensive hydrographic, geologic, ecological, and climatological data from publicly accessible sources, such as the National Land Cover Database (NLCD), Soil Survey Geographic Database (SSURGO), and Daymet. The Monitoring Trends in Burn Severity (MTBS) and Burned Area Emergency Response (BAER) burn severity mapping products were employed to assist in quantifying post-fire soil permeabilities. The Mckenzie River Watershed (Holiday Farm Fire in 2020), American River Watershed (Norse Peak Fire in 2017), Naches River Watershed (Schneider Springs Fire in 2021), and the Wenas Creek Watershed (Evans Canyon Fire in 2020) were selected as research areas, as the burned areas of the study fires are large (> 160 km^2, or 40,000 acres) and the land cover types and climates of the watersheds are representative in the Pacific Northwest. We specifically seek to address the following research questions:

1. How does fire-induced reduction in the leaf area index (LAI) affect post-fire evapotranspiration?
2. How does the burn severity of a wildfire event affect the post-fire peak flow discharges through the SWR effect?
3. What is the role of post-fire precipitation rate in impacting the post-fire peak discharges?
4. How does fire-induced infiltration change affect watershed function after a moderate-high severity fire?
5. How do fire-induced changes in Manning's n affect peak flow discharges after a low severity fire?

In this paper, we first introduce the study areas, the numerical model and its setup, how we represent fire impacts on soil and vegetation in the model, and the simulation scenarios for hypotheses testing in Section 2. In Section 3, we present and analyze the modeling results of the post-fire peak flow discharge and infiltration, and discuss the study limitations and key future work focuses, followed by conclusions in the final section.

2 Materials and Methods

2.1 Study sites

The focal watersheds in our study, subjected to recent wildfires in the Pacific Northwest, are the McKenzie River Watershed (impacted by the Holiday Farm Fire in 2020), the American River Watershed (impacted by the Norse Peak Fire in 2017), the Naches River Watershed (impacted by the Schneider Springs Fire in 2021), and the Wenas Creek Watershed (impacted by the Evans Canyon Fire in 2020). The watersheds of the American River, Naches River, and Wenas Creek reside within the Yakima River Basin, denoted by the Hydrologic Unit Code (HUC) 1703 in the State of Washington; whereas the McKenzie River Watershed is situated within the Willamette River Basin (HUC 1709) in the State of Oregon. Figure 1 illustrates their geographic positions within the Pacific Northwest. Importantly, the Holiday Farm Fire accounted for one of Oregon's 2020 megafires driven by compound extremes (Abatzoglou, Rupp, et al., 2021), causing over 600 km^2 of devastation in the McKenzie River valley (Robbins, 2021).

Burn severity data serves as an integral remote sensing mapping product to evaluate wildfire-induced effects on vegetation biomass due to the fire's heat pulse, rendering it a significant metric to quantify the fire impact (Parsons et al., 2010). We employed the Monitoring Trends in Burn Severity (MTBS) data to assess burn severity (Eidenshink et al., 2007) for the Holiday Farm Fire, Norse Peak Fire and the Evans Canyon Fire. The Burned Area Emergency Response (BAER) data (Parsons, 2003) was used for the Schneider Springs Fire. The key difference in the two data products is that BAER is used for immediate assessment purpose and MTBS is used for long-term monitoring purposes. The satelite images used in BAER are obtained as close to the fire events as possible, while the satelite images used in MTBS are of the next vegetation growing season (typically the next spring/summer).

Figure 2 depicts the burn severity statistics pertaining to the four studied wildfire events. Both the Holiday Farm Fire and Norse Peak fire-caused over 60% of the area to be subjected to moderate to high severity burning. Conversely, the Schneider Springs Fire and Evans Canyon Fire subjected approximately 40% and 15% of their areas to moderate to high severity burning, respectively. Details such as fire ignition dates, the size of the impacted areas, average daily total precipitation in the impacted watershed on an annual basis, and dominant land cover types are summarized in Table 1.

2.2 The burn severity dependent soil water repellency effect

To quantify the relationship between the strengths of the SWR effect and the hydrologic response is essentially to explain how the water conveyance capacity in porous media compares before and after combustion on top of the media. Soil burn severity, as a metric to assess the fire impact to soil, can be an appropriate metric in establishing the aforementioned relationship. However, existing studies show diverse conclusions (Vieira et al., 2015; Ebel & Moody, 2017; Robinne et al., 2020; Wagenbrenner et al., 2021; Carrà et al., 2021; Paul et al., 2022) and a comprehensive understanding on the relationship remains unclear. Despite the current inability and inaccuracy in quantitatively linking fire-induced SWR with burn severity in the hydrologic scientific community, some earlier studies have suggested that a reduction in hydraulic conductivity due to fire is inversely proportional to burn severity (Moody et al., 2015). Experiments by Hallema et al. (2018) pointed out the hydrophobic coating is highly related to the combustion temperature.

In both MTBS and BAER, burn severity is determined by the normalized burn ratio (NBR) and the differenced NBR (dNBR), whose practical value falls within the range of $(-2000, +2000)$ (Eidenshink et al., 2007). In this study, we applied a simplified linear relationship to quantify the SWR effect caused by wildfires:

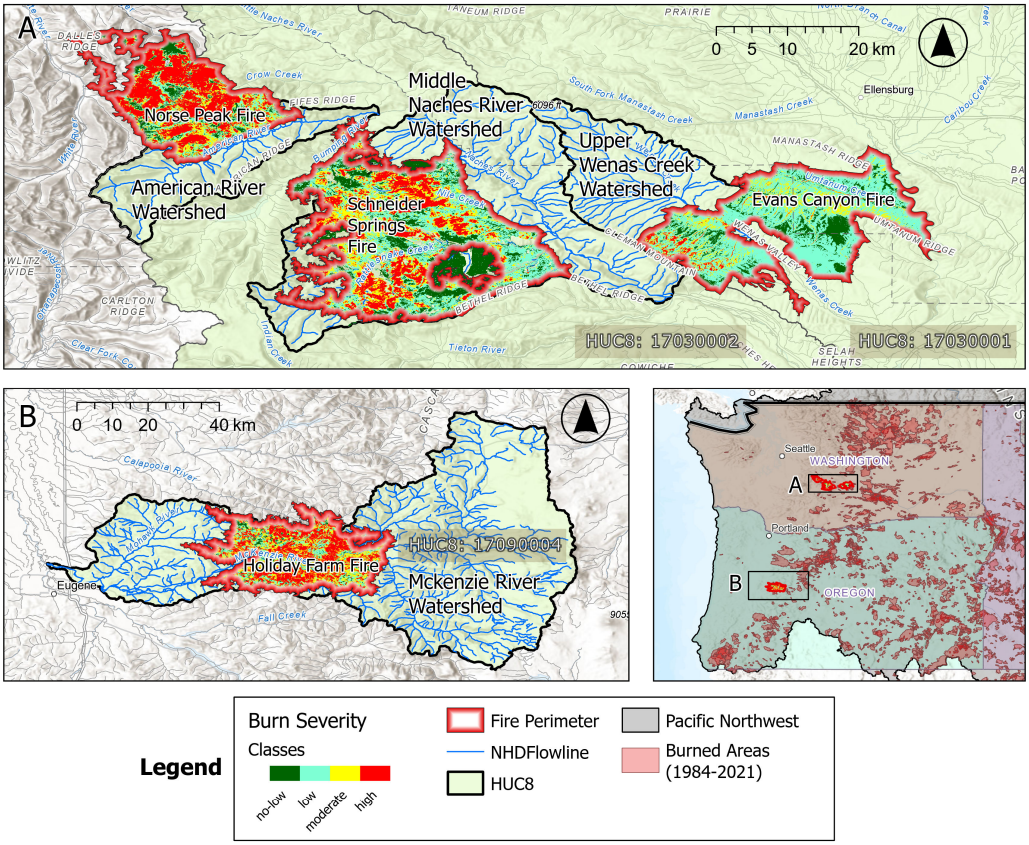

Figure 1. The fires and corresponding impacted watersheds within the Pacific Northwest. The McKenzie River Watershed in the State of Oregon is characterized as a subbasin (HUC8), while the American River Watershed, Naches River Watershed, and Wenas Creek Watershed in the State of Washington comprise multiple local sub-watersheds (multiple HUC12's). The perimeters of the fires and burn severity maps of the four scrutinized wildfires are shown.

Table 1. Basic information of the study wildfires and impacted watersheds

Wildfire (Impacted Watershed)	Ignition Date [mm/dd/yyyy]	Burned Area [km^2]	Annual Precip.* [mm] (climate classification†)	Dominant Land Cover Types‡
Holiday Farm Fire (Mckenzie River)	09/08/2020	642	1391 (Csb)	EF (80%) S/S (9%)
Norse Peak Fire (American River)	08/12/2017	188	868 (Dsc)	EF (87%) S/S (7%)
Schneider Springs Fire (Naches River)	08/04/2021	419	615 (Dsb)	EF (66%) S/S (21%) G/H (6%)
Evans Canyon Fire (Wenas Creek)	08/31/2020	281	406 (Dsb)	S/S (44%) EF (31%) G/H (22%)

*Annual avearge total precipitation
†Dominant Köppen–Geiger climate classification (Csb = temperate, dry and warm summer; Dsb = cold, dry and warm summer; Dsc = cold, dry and cold summer)
‡EF = Evergreen Forest; S/S = Shrub/Scrub; G/H = Grassland/Herbaceous

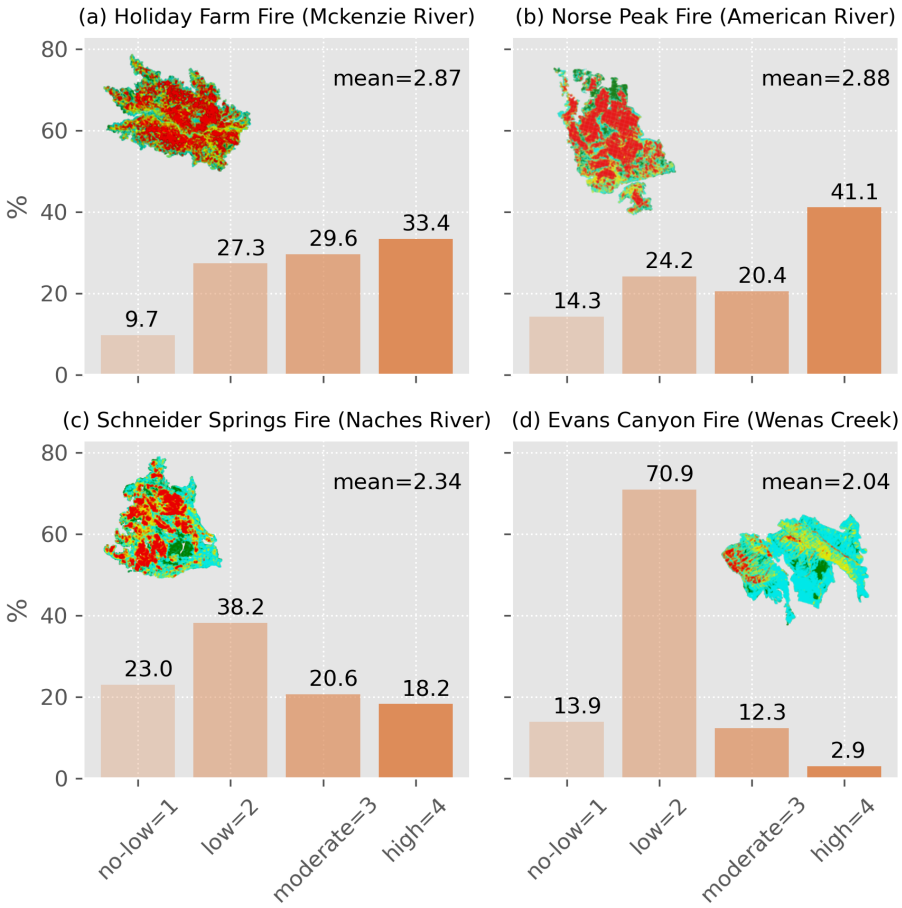

Figure 2. Burn severity statistics relative to the study wildfires: (a) the Holiday Farm Fire, with a mean burn severity of 2.87 and 63.0% of its area burned with moderate to high severity; (b) the Norse Peak Fire, with a mean of 2.88 and 61.2% of its area burned with moderate to high severity; (c) the Schneider Springs Fire, with a mean of 2.34 and 38.8% of its area burned with moderate to high severity; and (d) the Evans Canyon Fire, with a mean of 2.04 and a mere 15.2% of its area burned with moderate to high severity.

$$\text{Permeability}_{\text{post-fire}} = \text{Permeability}_{\text{pre-fire}} \cdot (1 - 20\% \cdot \text{Burn Severity}) \quad (1)$$

where *Burn Severity* can take integers 1, 2, 3, and 4 to represent no-low, low, moderate, and high burn severities, respectively.

In Figure 3, the pre-fire soil permeabilities are informed by the Soil Survey Geographic Database (SSURGO) database. Within the fire perimeter, after applying Equation 1, the topsoil permeability reduces to 80%, 60%, 40%, and 20% of its pre-fire value if the local burn severity is equal to 1, 2, 3, and 4, respectively. Thus, the ratio of the pre-fire topsoil permeability and the post-fire topsoil permeability represents exactly the burn severity integer indexes (see *Burn Severity* definition in Equation 1), as shown in the last panel of Figure 3. Note that the 0–5 cm soil layer is defined as the topsoil based on literature findings that the 0–5 cm layer is the most affected by fires (Roth et al., 2023).

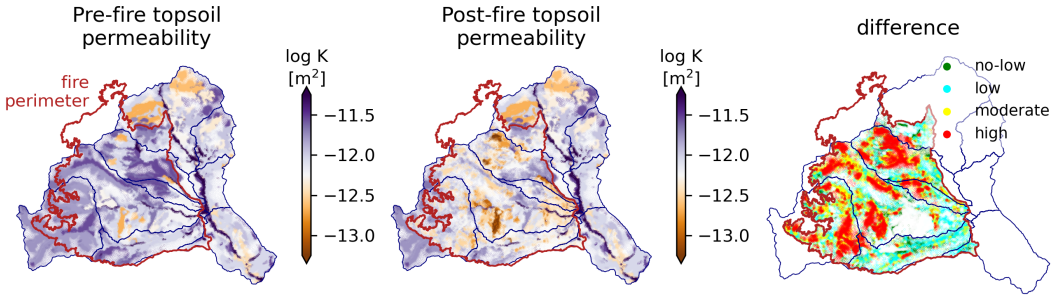

Figure 3. A graphic illustration of the post-fire topsoil permeability change. The Schneider Springs Fire in the Naches River Watershed is shown here as an example. The pre-fire soil permeability comes from the SSURGO database. The post-fire topsoil permeability has been updated using the burn severity map from the MTBS database.

The modifications in chemical and physical soil properties induced by fire were condensed into a single overarching effect, the SWR effect, accounting for the hydrophobic transformation of topsoil attributable to fire heat. This is a limitation engendered by the simplification of fire impact depiction in our model, since we did not conduct explicit and proactive simulations of the fire-originated ash layer. The ash layer is easily removed by the first post-fire flush, hence, the effects of the ash layer on the SWR effect is neglected. Anticipated future work includes integrating additional physics-based processes into the model to more accurately portray fire's impact on the underlying soil.

2.3 Model description

This study used the ATS version 1.4.1 (Coon et al., 2019, 2020). ATS is a high performance computing (HPC) code solving fully distributed and ecosystem-based integrated hydrology. It uses process kernels (PKs) and multi-process-couplers (MPCs) to allow custom coupling among different physical and biophysical processes. Here we used the watershed water balance MPC to couple the canopy water PK, the snow water PK, and the surface-subsurface flow MPC to simulate the integrated watershed hydrology. The surface-subsurface flow MPC couples the subsurface flow PK and the overland flow PK. ATS performance has been evaluated at different watersheds within the continental United States (Shuai et al., 2022; Bhanja et al., 2023). ATS divides the modeling domain into a terrain following two-dimensional (2D) surface domain and a three-dimensional (3D) subsurface domain, on which the diffusion wave equation for overland flow and the Richards equation for variably saturated groundwater flow are solved, respectively.

The water mass conservation equation on the surface domain reads:

$$\frac{\partial \Theta_s}{\partial t} + \nabla \cdot \mathbf{q_s} = \mathbf{Q_s} + \mathbf{Q_e} \tag{2}$$

where Θ_s is the mass of surface water per unit surface area; $\mathbf{q_s}$ is the overland flow rate per unit surface area; $\mathbf{Q_s}$ is the sources and sinks, including rainfall, snowmelt, evaporation and transpiration; and $\mathbf{Q_e}$ is the surface water-groundwater flux. If $\mathbf{Q_e} < 0$, water flows from surface to subsurface domain, i.e., infiltration.

Note that the canopy component of water storage is wrapped into the sources and sinks term, $\mathbf{Q_s}$, and the conservation of water in canopy is defined by,

$$\frac{d\Theta_{canopy}}{dt} = I - D_{snow} - D_{rain} - E_{canopy} \tag{3}$$

where Θ_{canopy} is the canopy water storage; I is the canopy interception and is associated with the leaf area index (LAI); D_{snow} and D_{rain} are the drainage of water from snow and rain from the canopy, respectively; and E_{canopy} is the evaporation of canopy water.

The water mass is written in terms of the water pressure p_s, the primary variable, through ponded depth h in the surface domain,

$$\Theta_s = \eta h \tag{4}$$

$$h = H\frac{(p_s - p_{atm})^2}{\rho g} \tag{5}$$

where η is the molar density of water; p_{atm} is the atmospheric pressure; ρ is the mass density of water; g is gravitational acceleration; and H is the Heaviside function to ensure non-negativity of water ponded depth.

The water flow rate on the surface domain is determined by the diffusion wave equation,

$$q_s = -\eta h\frac{h^{4/3}}{n\sqrt{|\nabla z|}}\nabla(h+z) \tag{6}$$

where n is the Manning's surface roughness coefficient and z is the elevation of the land surface.

In the 3D subsurface domain, the water mass conservation is governed by,

$$\frac{\partial \Theta_g}{\partial t} + \nabla \cdot \mathbf{q_s} = \mathbf{Q_g} \tag{7}$$

where Θ_g is the mass of groundwater per unit volume; q_s is the water flow rate in the subsurface domain; and Q_g is the sources/sinks term, representing processes such as injection or pumping wells.

The water pressure p_g is also used as the primary variable in the subsurface domain to solve the coupled water mass conservation by requiring $p_g|_{\partial\Omega} = p_s$. Subsurface water content is,

$$\Theta_g = \eta S_w \phi \tag{8}$$

and the Darcy's flow, q_g, is,

$$q_g = -\frac{\eta}{\mu} k_r K (\nabla p + \rho g z) \tag{9}$$

where ϕ is the porosity of the medium; S_w is the water saturation; μ is the water viscosity; k_r is the relative permeability; and K is the absolute permeability.

2.4 Model setup and simulated scenarios

To drive the integrated hydrologic model, an extensive set of hydrography, digital elevation model (DEM), land cover, subsurface material structures/properties, and meteorological data are essential. The Watershed Workflow package (Coon & Shuai, 2022) was employed to systematically retrieve and compile the requisite input data from publicly available sources spanning various data-providing and managing agencies such as the U.S. Geological Survey (USGS), U.S. Department of Agriculture (USDA), and others. A comprehensive inventory detailing the input data utilized and their respective sources can be found in Table A1 in Appendix A.

The computational meshes (triangular prism 3D cells) are generated also using Watershed Workflow. A 3D mesh is vertically extruded from a terrain following 2D triangular mesh generated through Delaunay triangulation, leveraging the `Triangle` library (Shewchuk, 2002), a Delaunay triangulator widely applied in computational physics. Through the mesh extrusion, each soil column contains 15 layers with a total thickness ranging from 40-50 m, determined by the depth to bedrock data in the SoilGrids database (Poggio et al., 2021). The 2D and 3D mesh refinements are done along stream networks informed by the NHDPlus High Resolution dataset (U.S. Geological Survey, 2023b), and in the top 2 meters of soil, respectively. The smallest triangle area is approximately 20,000 m^2 in the Mckenzie River Watershed and approximately 5,000 m^2 in the other three watersheds, resulting in approximately 1.8 million 3D cells in the Mckenzie River Watershed and approximately 600 thousands to 1 million 3D cells in the other three watersheds.

Figure 4 shows an example setting up the model for one of the study watersheds, the Naches River Watershed. The canopy biophysical processes and ground surface energy balance are computed on the surface domain of the model, thus the associated parameters (e.g., rooting profiles, photosynthetic parameters, albedo, and others) are stored in 2D cells with spatial variation. The LAI of each plant functional type is extracted from the Moderate Resolution Imaging Spectroradiometer (MODIS) dataset and has both temporal and spatial variations. In each 3D cell, the subsurface material properties, e.g., permeability and porosity, are assigned with the values from the national databases as *a priori* information (Bhanja et al., 2023). Nonetheless, we acknowledge that the ATS-simulated fire-affected watershed hydrology necessitates reinforcement from *in-situ* post-fire soil data acquisition through field campaigns, which are both logistically challenging and exceptionally valuable.

The meteorological forcing data is from the Daymet dataset, which provides 1 km $\times$ 1 km resolution gridded precipitation, air temperature, incoming shortwave radiation, and vapor pressure data across continental North America beginning in 1980. Rain and snow are partitioned from precipitation based on the air temperature. The gridded transient forcing data is mapped onto the computational mesh at each time step, which varies from several minutes to approximately 1 hour, depending on the Courant–Friedrichs–Lewy (CFL) condition. Linear interpolation on the Daymet dataset is performed to provide subdaily forcing data. We recognize the crucial nature of subdaily precipitation data when considering post-fire watershed hydrology. Existing research pertaining to fire impacts has illuminated that the initial 30 minutes of a precipitation event exert the most influence on post-fire surface runoff (Moody, 2012; Ebel et al., 2012; Murphy et al., 2015).

Nonetheless, to effectively tackle spatial heterogeneity at the watershed or sub-basin scales, we opted for the Daymet dataset over other publicly available meteorological forcing datasets with superior temporal resolution but inferior spatial resolution. A comparative study by Shuai et al. (2022) of three publicly accessible gridded meteorological forcing datasets, namely Daymet (used in this study), the Parameter-elevation Regressions on Independent Slopes Model (PRISM), and the North American Land Data Assimilation System (NLDAS), concluded that a higher spatial resolution is more advantageous for scientific enquiries involving significant spatial heterogeneity within the framework of ATS watershed hydrology simulations. In scenarios where a higher spatial resolution is indispensable, employing statistical downscaling techniques (Rastogi et al., 2022) on meteorological forcing data may become a necessity for executing fire hydrologic impact assessments at a finer temporal resolution, to be addressed in future work.

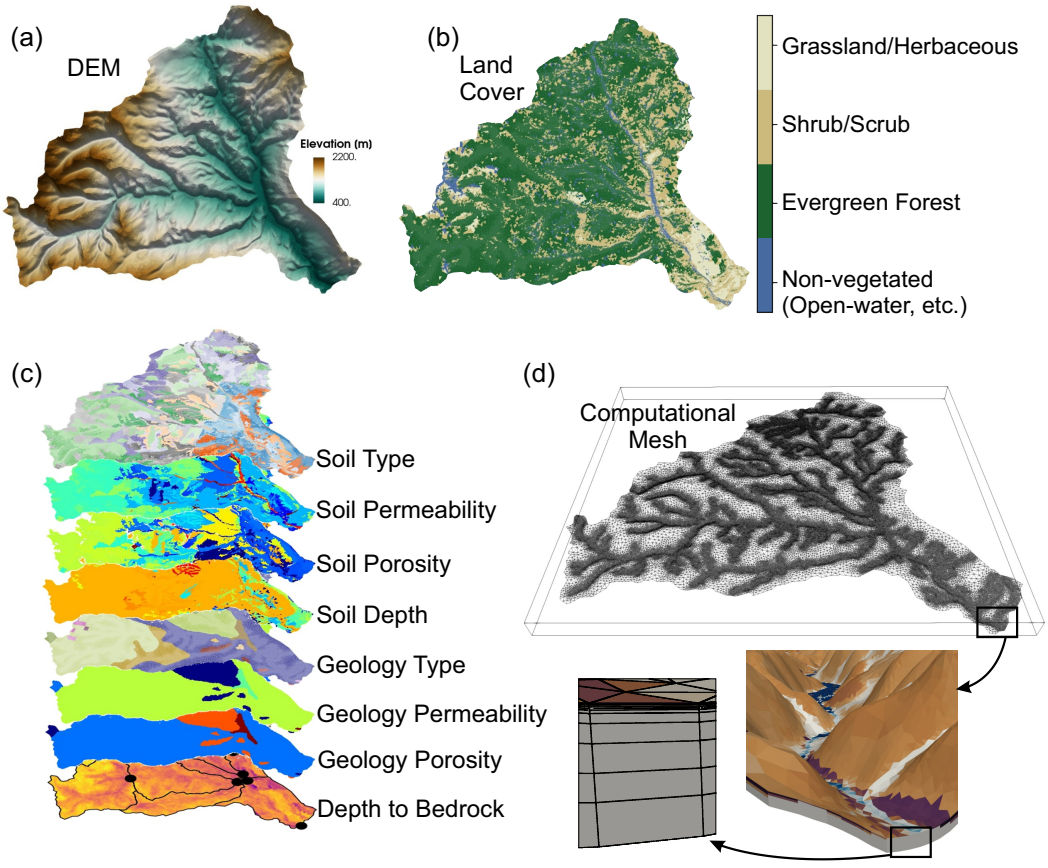

Figure 4. Key components of model setup for the Naches River Watershed. (a) DEM, (b) land cover type, (c) soil and geology properties, and (d) the 3D computational mesh.

In each watershed, a 500-year simulation using the annual mean precipitation rate (rainfall only) was first performed as the model cold spin-up. Next, using the final steady-state model output from the cold spin-up as the initial condition, a 40-year simulation was performed to reach the cyclic steady state using "typical year" meteorological forcing (Figure 5) and LAI data, as the model hot spin-up. Seasonal variabilities of surface water and groundwater flow as well as evaporation and transpiration are the featured results from the model hot spin-up simulations. Finally, transient simulations with meteorological forcing data were initialized using the model output of the final time step in model hot spin-up.

The duration of the transient run is constrained by the availability of two dynamic raster datasets, namely meteorological forcing data from Daymet covering the period from 1980 to 2021 and LAI data from MODIS spanning from 2002 to 2023. Consequently, we initiated the transient simulations on October 1, 2002 and concluded them on December 31, 2021, in the American River Watershed, Naches River Watershed, and Wenas Creek Watershed. However, in the case of the McKenzie River Watershed, the temporal extent was curtailed to October 1, 2012 to December 31, 2021, due to the substantial computational burden arising from its large size.

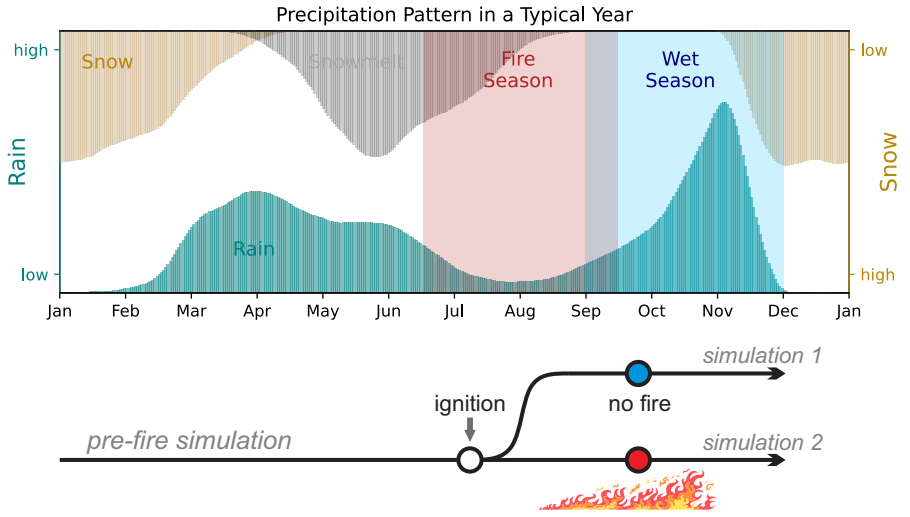

Figure 5. Watershed-averaged precipitation pattern in a "typical year" in the Pacific Northwest. Wildfire season is from late-June to mid-September. All four wildfires in this study occurred in the typical wildfire season in the Pacific Northwest. The wet season is from early-September to late-November. Snow season is from late-November to late-March of the next year. Two parallel simulations, with and without the fire-caused SWR effect, are performed after fire ignition.

As shown in Figure 5, the Pacific Northwest summer wildfire season is typically followed by a wet season in the fall, which explains the increased risks for post-fire flooding and debris flow hazards (Wall et al., 2020). After a fire ignition date, two parallel simulation are performed to compare with and without the fire-caused SWR effect on watershed hydrology (Figure 5).

The evaluation of the hydrologic response of a watershed to a wildfire disturbance is a typical disturbance response test in dynamical systems theory. Hence, except for the post-fire wet season in the actual fire year (e.g., 2021 for the Schneider Springs Fire in the Naches River Watershed), the fire impacted watershed hydrology is also examined using historical wet seasons from 1980 and 2021. Figure 6a displays the annual pattern of daily total rainfall in the Naches River Watershed (as an example). Figure 6b-c zoom in to the wet season in between September 1 and November 30 and highlight the daily total rainfall in wet seasons in 2021 and 2006, respectively. The post-fire wet season in the actual fire year, 2021, did not encounter a historically large rainfall event. Thus, the historical greatest daily rainfall event that occurred in 2006 was used to test the watershed response to the fire-caused SWR effect under extreme meteorological forcing. Similarly, the top 10 greatest daily rainfall events were examined (Table B1 in Appendix B). The simulated scenarios are listed in Table 2.

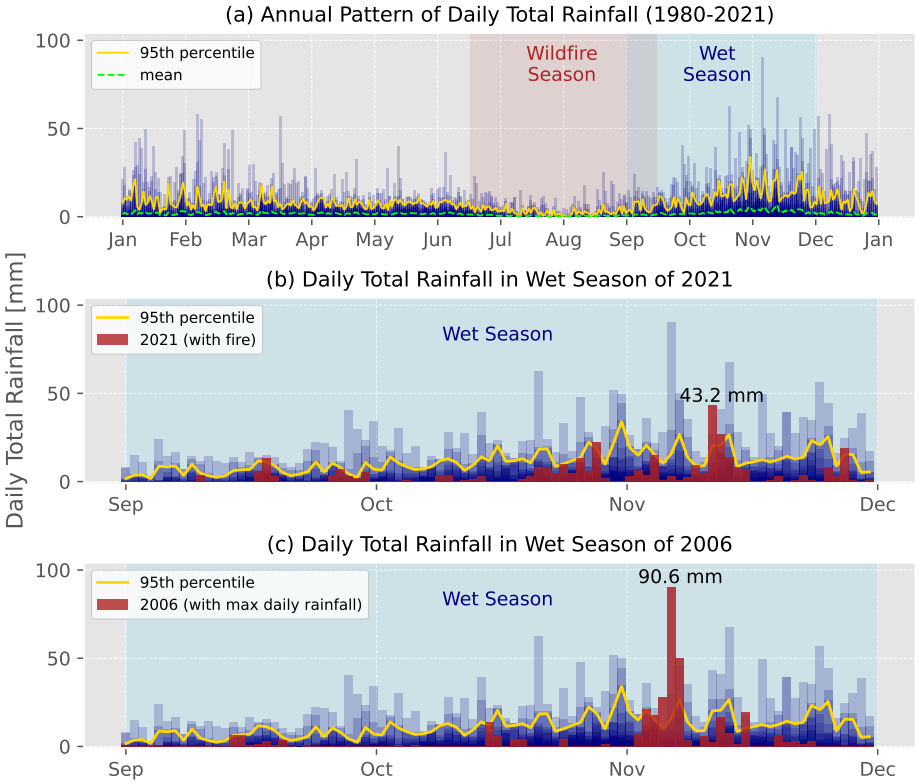

Figure 6. The historical rainfall events in wet season in the Naches River Watershed as an example. (a) Annual pattern of daily total rainfall in the Naches River Watershed. The blue bars are the 1980 to 2021 daily total rainfall. The mean and the the 95th percentile are plotted by the yellow dashed line and red soil line. (b) The red bars highlight the daily total rainfall in 2021 wet season. The Schneider Springs Fire occurred in the wildfire season of 2021. (c) The red bars highlight the daily total rainfall in the 2006 wet season, when the greatest daily rainfall occurred.

Table 2. Simulated scenarios

Scenario	Time Period [mm/dd/yyyy]	Fire-caused LAI reduction	Fire-caused SWR effect	Meteorological Forcing Data*	Fire-caused Manning's n Reduction
Mckenzie-long	10/01/2012–12/31/2021	Yes	No	P_0	No
American-long	10/01/2002–12/31/2021	Yes	No	P_0	No
Naches-long	10/01/2002–12/31/2021	Yes	No	P_0	No
Wenas-long	10/01/2002–12/31/2021	Yes	No	P_0	No
Mckenzie-l-N**	09/08/2020–12/01/2020	Yes	No	$P_0, P_1, ..., P_{10}$	No
Mckenzie-ls-N	09/08/2020–12/01/2020	Yes	Yes	$P_0, P_1, ..., P_{10}$	No
American-l-N	08/12/2017–12/01/2017	Yes	No	$P_0, P_1, ..., P_{10}$	No
American-ls-N	08/12/2017–12/01/2017	Yes	Yes	$P_0, P_1, ..., P_{10}$	No
Naches-l-N	08/04/2021–12/01/2021	Yes	No	$P_0, P_1, ..., P_{10}$	No
Naches-ls-N	08/04/2021–12/01/2021	Yes	Yes	$P_0, P_1, ..., P_{10}$	No
Wenas-l-N	08/31/2020–12/01/2020	Yes	No	$P_0, P_1, ..., P_{10}$	No
Wenas-ls-N	08/31/2020–12/01/2020	Yes	Yes	$P_0, P_1, ..., P_{10}$	No
Wenas-lsm	08/31/2020–12/01/2020	Yes	Yes	P_0	Yes
American-nl	08/12/2017–12/01/2017	No	No	P_0	No

* P_0 is the meteorological forcing data in the post-fire wet season in the actual fire year; $P_1, P_2, ..., P_{10}$ are the 10 greatest daily rainfall wet seasons from historical data.
** N is an integer from 0 to 10 to represent P_0–P_{10}, respectively.

The simulations were performed using 256 to 1,024 cores on Cori (Intel Xeon E5-2698 v3) and Perlmutter (AMD EPYC 7763), two National Energy Research Scientific Computing Center (NERSC) supercomputers.

2.5 Model performance evaluation metrics

Model evaluation was performed by comparing to both simulated streamflow discharge and total evapotranspiration (ET) with observations. Daily continuous streamflow data at the outlets of the Mckenzie River Watershed and the American River Watershed for 1980 to 2021 were obtained from the USGS National Water Information System (NWIS). Since no observations are available in the Naches River Watershed and the Wenas Creek Watershed, river flow discharges from the National Water Model (NWM) are used for model to model comparison. The NWM is a specific configuration of WRF-Hydro covering the entire continental United States, simulating hourly surface and subsurface hydrologic processes. The backbone of the surface process includes Noah-MP simulating land surface process, a quasi-3D flow module simulating the subsurface flow, and a 2D diffusion wave equation simulating surface water. The resulting overland flows are then aggregated to the catchment streamflow using a Muskingum scheme, based on NHDPlus catchment delineation. Lastly, the 8-day averaged gap-filled ET from the MODIS database (product name: MOD16A2 V6) is used for the total ET.

We used the coefficient of determination (R^2), the Nash-Sutcliffe Efficiency (NSE) (Equation 10) and the modified Kling-Gupta efficiency (mKGE) (Equation 11-12) as the key metrics for evaluating the model performance (Nash & Sutcliffe, 1970; Gupta et al., 2009; Kling et al., 2012):

$$NSE = -(\frac{\mu_{sim} - \mu_{obs}}{\sigma_{obs}})^2 - (\frac{\sigma_{sim}}{\sigma_{obs}})^2 + \frac{2\sigma_{sim}\rho}{\sigma_{obs}} \tag{10}$$

$$KGE = 1 - \sqrt{(R-1)^2 + (\frac{\sigma_{sim}}{\sigma_{obs}} - 1)^2 + (\frac{\mu_{sim}}{\mu_{obs}} - 1)^2} \\ = 1 - \sqrt{(R-1)^2 + (\gamma - 1)^2 + (\beta - 1)^2} \tag{11}$$

$$mKGE = \frac{KGE + \sqrt{2} - 1}{\sqrt{2}} \tag{12}$$

where *sim* and *obs* are the simulated and observed time series (of streamflow discharge and total ET in this study), respectively; σ and μ represent standard deviation and mean, respectively; ρ is the Pearson correlation coefficient; R is the coefficient of correlation; γ is the variability ratio; and β is the bias ratio. Note that the key difference between NSE and KGE/mKGE is that KGE/mKGE is not derived from the mean squared error—it simply uses the L^2 norm of correlation, standard deviation, and bias. Both NSE and mKGE lie in $(-\infty, 1]$. Negative NSE or mKGE values imply poor model performance. When $NSE = 0$ or $mKGE = 0$, the model performance is same as predictions using the mean of the observations, i.e., μ_{obs}. Model prediction is perfect when $NSE = 1$ or $mKGE = 1$.

3 Results and Discussion

3.1 Model performance evaluation

The model showed generally good performance in simulated flow discharge compared to observed flow discharge (USGS) and NMW-simulated flow discharge (Figure 7). The modeling result on flow discharge at watershed outlet in the American River Watershed is more accurate than in the other three watersheds. The R^2, NSE and mKGE scores are 0.708, 0.576 and 0.742, respectively, indicating outstanding model performance (Figure 7b). In the Mckenzie River Watershed and Naches River Watershed, the R^2 scores are 0.749 and 0.506, the NSE scores are 0.232 and 0.414, and the mKGE scores are 0.436 and 0.608, respectively (Figure 7a and 7c). The model performance on flow discharge in these two watersheds is good, but worse than in the American River Watershed. The performance difference can be explained by the watershed size differences—the American River Watershed modeling domain is significantly smaller, at only 6.9% and 26.5% of the size of the Mckenzie River Watershed and the Naches River Watershed modeling domains. Fully distributed hydrologic models like ATS commonly perform better at smaller spatial scales than at larger spatial scales (Merz et al., 2009), due to larger uncertainties and increased challenges in calibrating spatially varying parameters.

Though model correctly predicts the basic seasonable variations, the simulated flow discharge at the watershed outlet in the Wenas Creek Watershed shows the worst performance of the studied watersheds. The R^2, NSE, and mKGE scores are 0.159, 0.233, and 0.228, respectively. The scatter plot in Figure 7d shows a large deviation when ATS predicts near zero flow discharge. However, the NWM predicts higher flow discharge. This discrepancy may explain the low performance scores of ATS—the base flow predicted by ATS is relatively inaccurate compared to its peak flow predictions, implying inaccuracy in ET predictions during hot and dry days. The varibility ratio $\gamma = 1.382$ and the bias ratio $\beta = 0.702$, implying that ATS streamflow predictions have larger standard deviation and lower mean compared to the NWM predictions, caused by the low performance of ATS in base flow predictions. Note that the NWM flow discharge result in the Wenas Creek Watershed is assumed as the ground truth, which may bring uncertainties to evaluating ATS modeling results.

Figure 8 shows the ATS model performance for watershed-averaged total ET in the study watersheds. In the Mckenzier River Watershed, American River Watershed, and

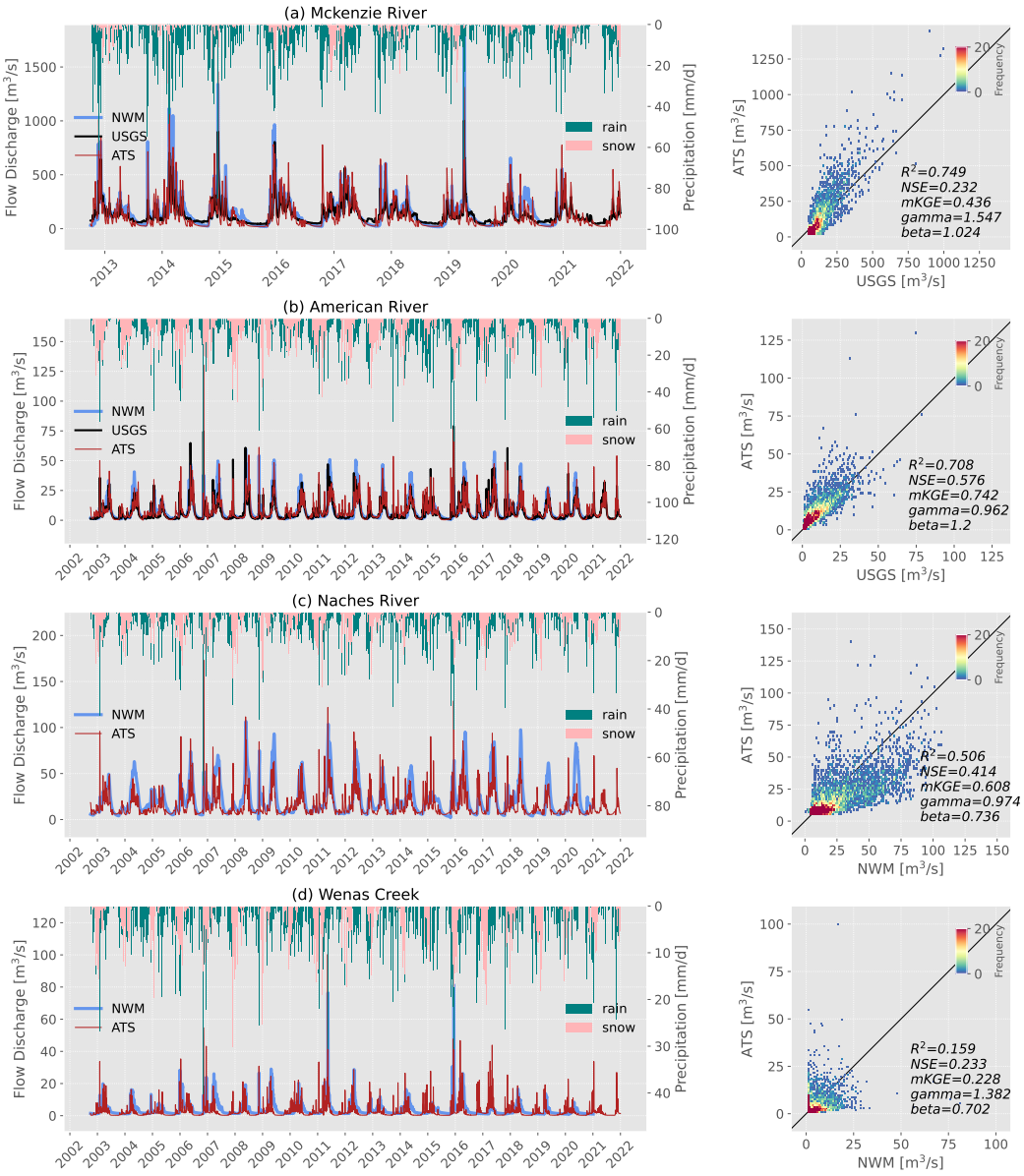

Figure 7. ATS model performance of flow discharge in the (a) Mckenzie River, (b) American River, (c) Naches River, and (d) Wenas Creek.

Naches River Watershed, the R^2, NSE, and mKGE scores are all greater than 0.7, suggesting that model predictions are accurate on watershed-averaged total ET by ATS in these three watersheds. However, the ATS predicted watershed-averaged total ET in the Wenas Creek Watershed is underestimated in winter seasons, leading to lower performance scores compared to the other three watersheds. The R^2, NSE, and mKGE scores are 0.689, 0.557, and 0.405, respectively. A difference in the dominant land cover type between the Wenas Creek Watershed and the other three watersheds may explain the ATS predicted ET performance difference. As seen in Table 1, the dominant land cover type in the Wenas Creek Watershed is shrub/scrub (44%), evergreen forest (31%) and grassland/herbaceous (22%). In the other three watersheds, evergreen forest is greatly dominant (66%–87%). This discrepancy suggests that the biophysical parameters used to compute evaporation and transpiration (e.g., Priestley-Taylor constants, LAI, etc.) are less accurate for shrub/scrub than evergreen forest, even though they are both referenced from the CLM 4.5 technical notes (Oleson et al., 2010).

In general, the ATS modeling results compare well with both the USGS observed flow discharges and the NWM predicted flow discharges. This agrees with the results of Bhanja et al. (2023) that ATS has reasonably good performance without modeling domain specific calibration when using only *a priori* information. Through the long term pre-fire simulations, we are also able to visualize the watershed hydrologic conditions (topsoil saturation and surface water ponded depth) on the fire ignition dates and the first significant rainfall event dates (Figure 9).

3.2 Watershed average evapotranspiration is reduced after high burn severity wildfires

The research question, *"how much does the fire-caused LAI reduction affect the post-fire evapotranspiration"*, is analyzed through the Norse Peak Fire within the American River Watershed. Figure 10 shows two concurrent five-year simulations that span from 2017—the inception of the Norse Peak Fire—to 2022. These portrayed the simulation scenarios American-l and American-nl, which are delineated in Table 2.

The time series of simulated ET utilizing the LAI data extracted from the MODIS dataset are displayed in Figure 10a. The red dashed and gold dotted curves denote two predominant land cover classes within the American River Watershed, evergreen forest and shrub/scrub, respectively. In the aftermath of the Norse Peak Fire in 2017, a decrease followed by a recovery phase was observed in the LAI for both evergreen forest and shrub/scrub over the next four years. This dynamic shift had a direct influence on the simulated ET, as depicted by the green solid curve. The simulated ET registered a decline during 2018-2020 and an approximate restoration to its antecedent, pre-fire condition by 2021.

To explore the influence of fire-induced LAI diminution on simulated ET, we replicated the 2017 LAI data for both evergreen forest and shrub/scrub in subsequent years, specifically 2018-2021. This simulation scenario represents a theoretical condition, disregarding any vegetation impact due to the Norse Peak Fire in 2017. As demonstrated in Figure 10b, the simulated ET retains identical seasonal magnitudes. A comparative analysis of simulation outcomes from scenarios American-l and American-nl provides direct evidence that the watershed-averaged ET is significantly altered by the reduction in LAI resulting from a high burn severity fire.

3.3 High burn severity wildfires cause increased post-fire peak flow discharges

We found that high burn severity fires cause increased post-fire peak flow discharges, while low burn severity fires can hardly yield similar impacts. Figure 11 shows that the

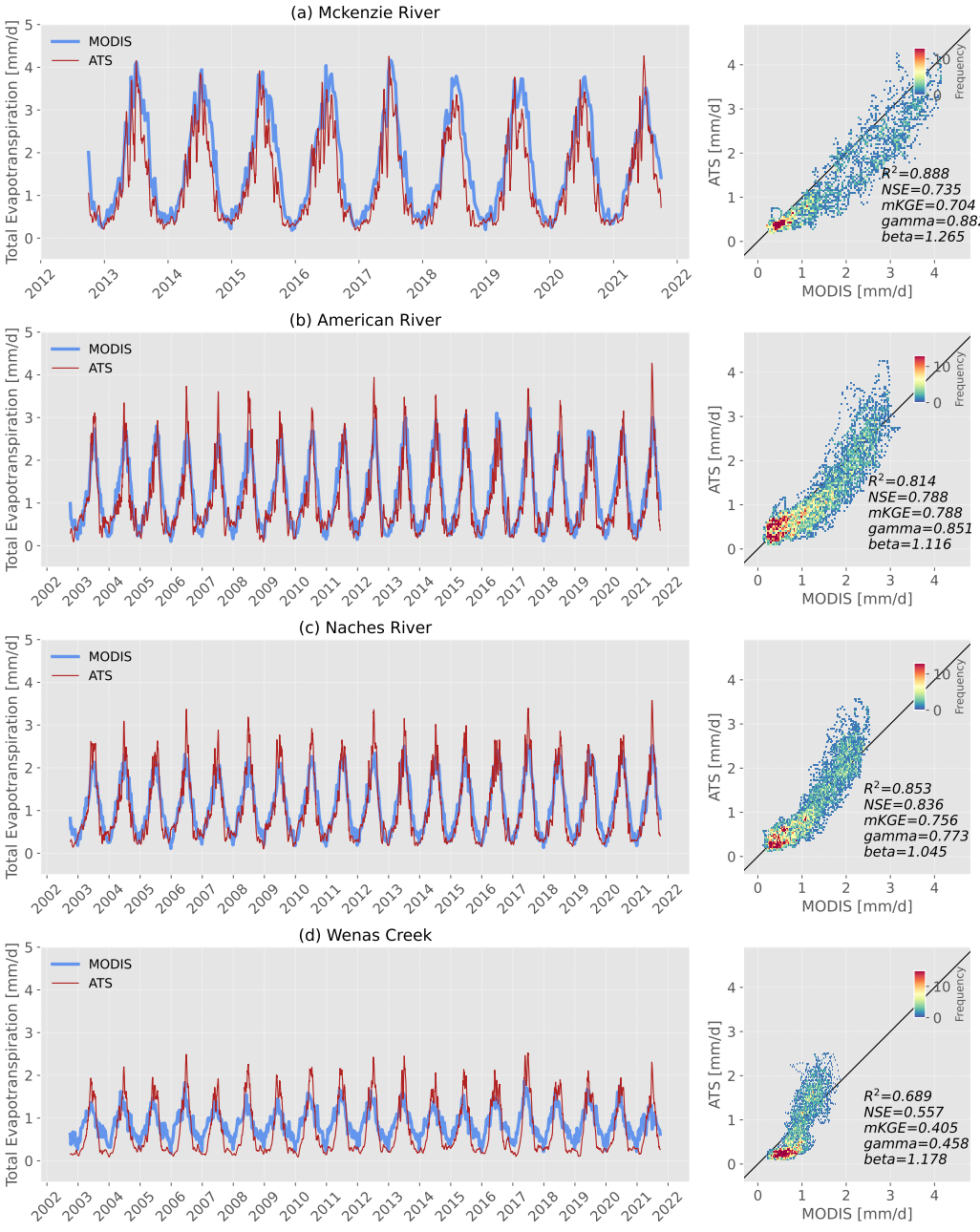

Figure 8. ATS model performance on watershed-averaged total evapotranspiration in the (a) Mckenzie River, (b) American River, (c) Naches River, and (d) Wenas Creek.

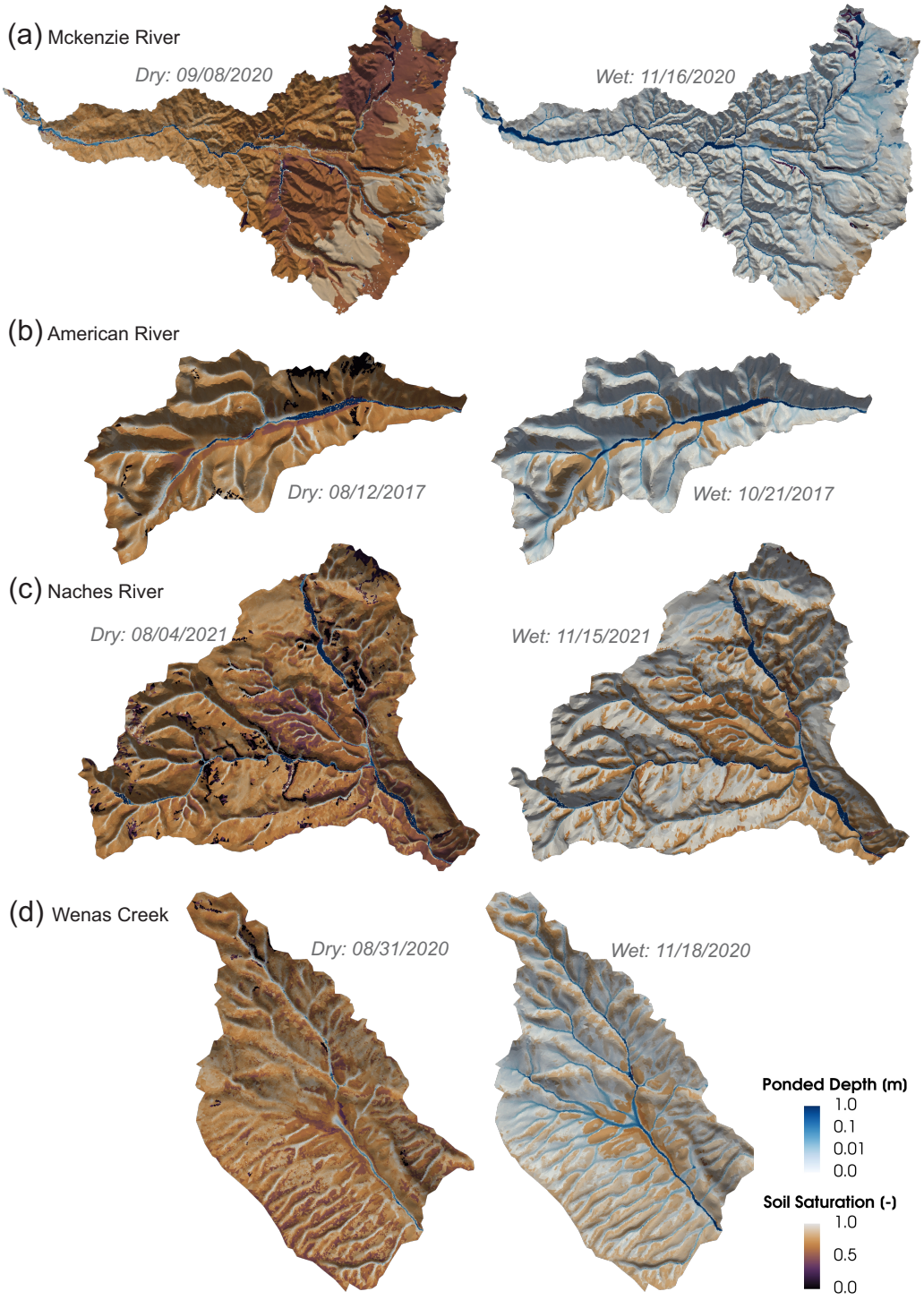

Figure 9. Watershed dry conditions on the fire ignition dates and wet conditions during the first significant post-fire precipitation events. (a) 09/08/2020 (dry) and 11/16/2020 (wet) in the Mckenzie River Watershed, (b) 08/12/2017 (dry) and 10/21/2017 (wet) in the American River Watershed, (c) 08/04/2021 (dry) and 11/15/2021 (wet) in the Naches River Watershed, and (d) 08/31/2020 (dry) and 11/18/2020 (wet) in the Wenas Creek Watershed.

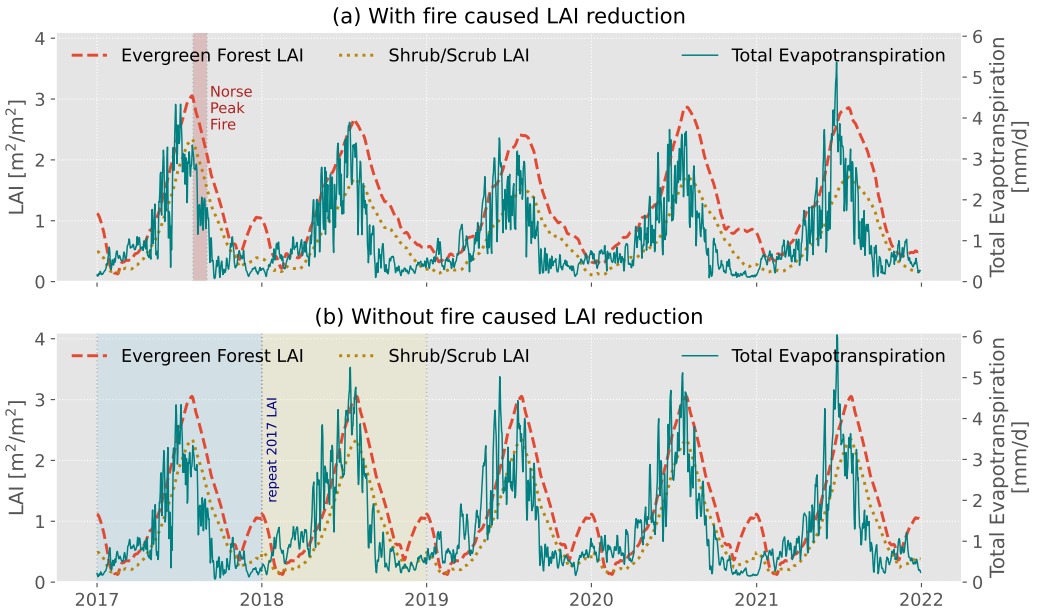

Figure 10. The comparison between scenarios (a) with and (b) without the fire caused LAI reduction and its affect on the simulated ET.

modeling results for the simulation scenarios Mckenzie-l and Mckenzie-ls (Figure 11a), American-l and American-ls (Figure 11b), Naches-l and Naches-ls (Figure 11c), and Wenas-l and Wenas-ls (Figure 11d). Comparison between Figure 11a-c and Figure 11d reveals the burn severity plays a key role in post-fire peak discharge increases, since the mean burn severities of the Holiday Farm Fire, the Norse Peak Fire, and the Schneider Springs Fire are 2.87, 2.88, and 2.34, respectively, while the mean burn severity of the Evans Canyon Fire is 2.04. The post-fire peak flows in the Mckenzie River Watershed, Ameircan River Watershed and the Naches River Watershed increased 21-34%, owing to the fire caused SWR effect. In the Wenas Creek Watershed, the post-fire peak flow discharge increase is merely 2%, implying no significant fire impact through the SWR effect.

3.4 Increased peak flow discharges due to high-burn severity fires are intensified by increased post-fire precipitation

Another key finding of our study is that high burn severity fires-caused increased peak flow discharges immediately post-fire are intensified by higher precipitation rates; while low burn severity fire is insensitive to the increased post-fire higher precipitation rates. Figure 12 shows the modeling results from the simulation scenarios: Mckenzie-l-1 to -10 and Mckenzie-ls-1 to -10 (Figure 12a), American-l-1 to -10 and American-ls-1 to -10 (Figure 12b), Naches-l-1 to -10 and Naches-ls-1 to -10 (Figure 12c), and Wenas-l-1 to -10 and Wenas-ls-1 to -10 (Figure 12d). With respect to a fire of certain burn severity statistics and spatial distribution, a reduced post-fire precipitation rate inflicts minimal hydrologic disturbance, whereas a higher post-fire precipitation rate culminates in significant post-fire peak flows. This indicates that fire-induced watershed hydrology alterations are exacerbated by increased post-fire precipitation rates. However, in the Wenas Creek Watershed, even a threefold increase in post-fire precipitation rate did not yield significant differences in hydrologic response when comparing scenarios with and without the fire-induced SWR effect, a consequence of the low burn severity of the Evans Canyon Fire.

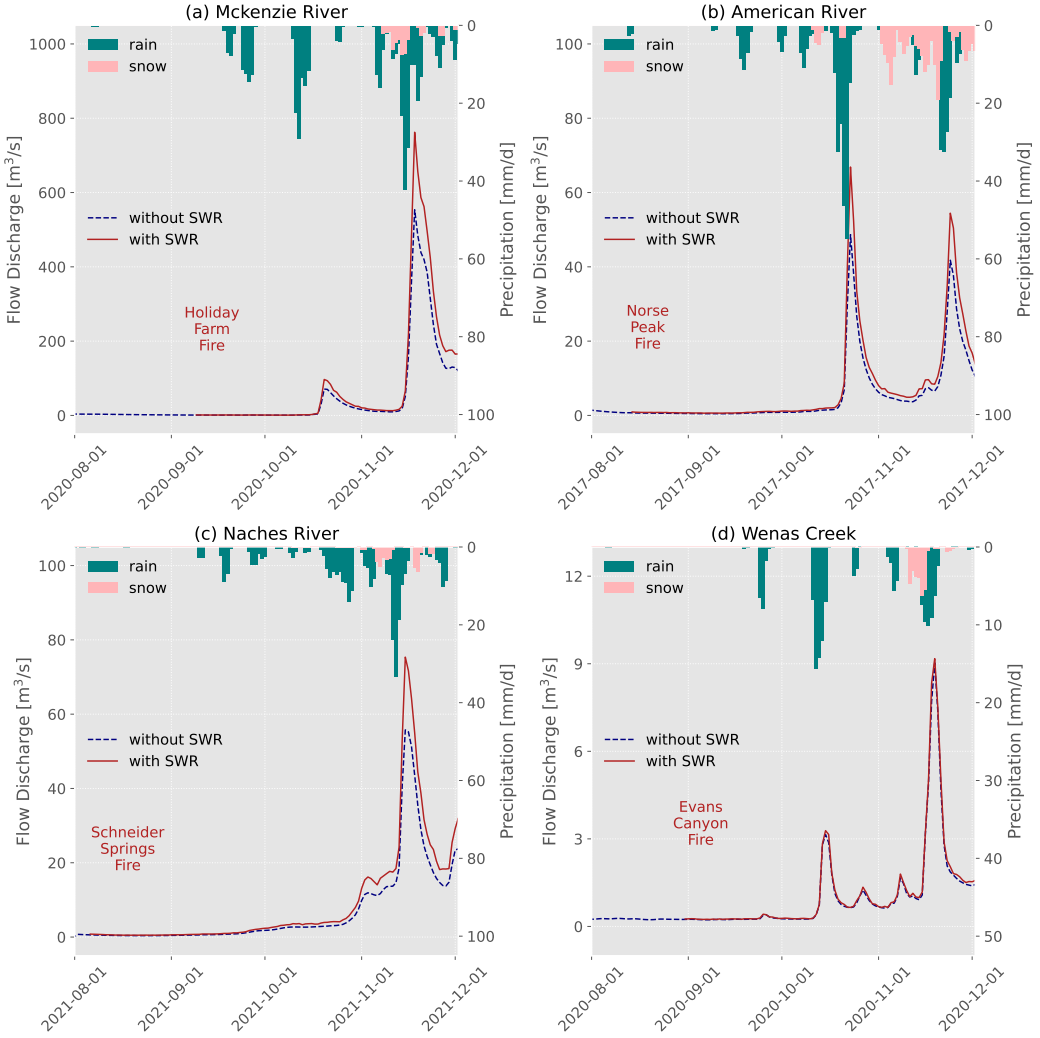

Figure 11. Post-fire peak discharges with and without the fire-caused SWR effect in (a) the Mckenzie River Watershed, (b) the American River Watershed, (c) the Naches River Watershed, and (d) the Wenas Creek Watershed.

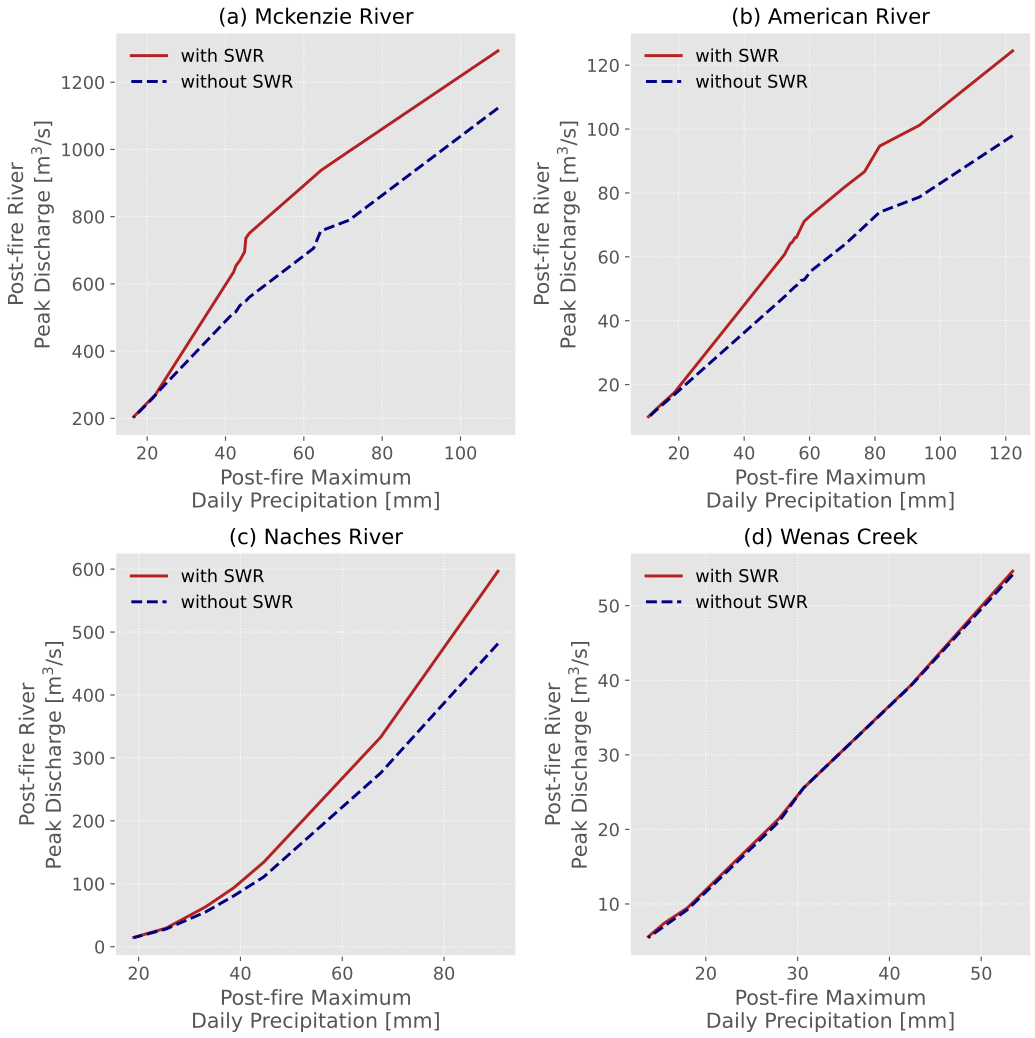

Figure 12. Correlation between the post-fire peak discharge with and without the fire-caused Soil Water Repellency effect and the post-fire maximum daily precipitation in (a) the Mckenzie River Watershed, (b) the American River Watershed, (c) the Naches River Watershed, and (d) the Wenas Creek Watershed.

3.5 High burn severity wildfires suppress infiltration through soil water repellency (SWR) effect

We used the Norse Peak Fire in the American River Watershed as a case study to answer the research question, *"how does the infiltration changed by the fire caused SWR effect after a moderate-high severity fire"*. This decision was predominantly driven by the superior performance of the model concerning surface water flow discharge and ET among all watersheds incorporated in this study. The investigations revealed that fires with high burn severity have the potential to inhibit infiltration due to the SWR effect.

The time series of the magnitudes of the watershed maximum infiltration in scenarios with and without the fire-induced SWR effect are shown in Figure 13a. By incorporating the influence of the fire-induced SWR effect, a noticeable decrease in the magnitudes of infiltration is observed. A mean reduction of 38% in the infiltration rate within the American River Watershed was evident. The two top-view panels in Figure 13b and 13c elucidate the spatial distribution of infiltration within the American River Watershed, both with and without the influence of the fire-induced SWR effect. Subsequent to the Norse Peak Fire in 2017, the first substantial precipitation event in the wet season presented a higher infiltration rate than years with an active fire-induced SWR effect. This observation can be attributed to the fact that the fire-induced hydrophobic layer on the topsoil impedes infiltration.

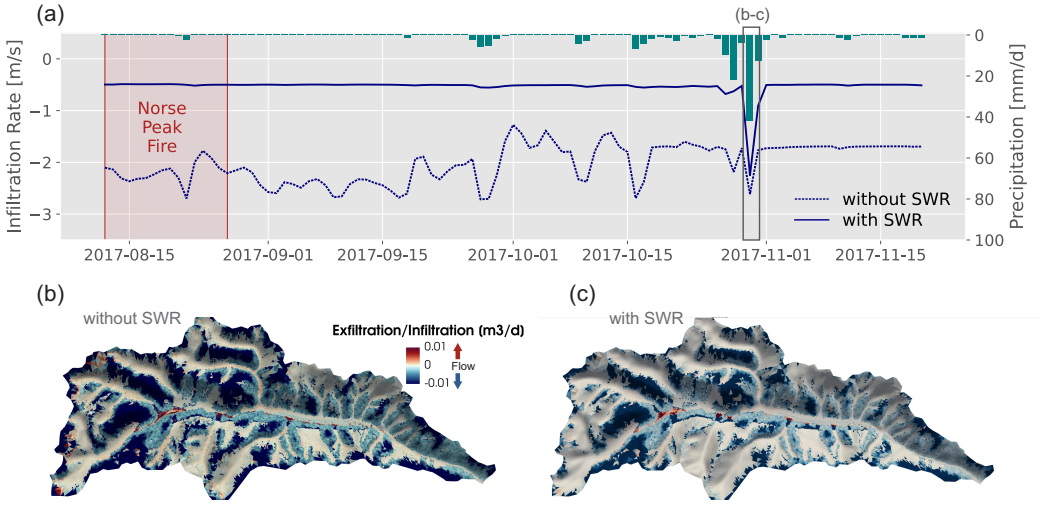

Figure 13. (a) The watershed maximum infiltration rate in the American River Watershed after the Norse Peak Fire for the two scenarios, without and with the SWR effect. (b-c) The spatial distribution of infiltration in the American River Watershed on the day with first significant precipitation event after the Norse Peak Fire for the two scenarios, without and with the SWR effect.

3.6 Fire-caused Manning's n reduction causes increased post-fire peak flow discharges

We addressed research question, *how does the fire caused Manning's n reduction affect the post-fire peak flow discharges after a low severity fire*, by studying the Evans Canyon Fire-affected Wenas Creek Watershed. This area was selected due to previous findings that suggested that the SWR effect does not exert a significant influence on the post-fire peak flow discharge, thereby necessitating an examination of the sensitivity of

the Manning's n reduction on the post-fire peak flow discharge. As delineated in Figure S3 in the Supporting Information (SI) document, both the dashed blue and solid red curves symbolize scenarios (Wenas-l and Wenas-ls) previously depicted in Figure 12d. The green solid-dotted curve shows the impact of Manning's n on the post-fire peak flow discharge. The decrease in the Manning's coefficient as a consequence of vegetation loss, attributable to fire, led to increases in post-fire peak flows. This is supported by a 5-19% escalation detected during several post-fire precipitation events, as indicated in Figure S3 in the SI. Of note, the reduction in Manning's n attributed to the fire is not solely in river channels, but is distributed across all the combusted regions to account for the loss of vegetation. The influence of Manning's n on surface runoff is unsurprising, given its role as a paramount factor in determining flow discharge within the overland flow model that solves the diffusion wave equation.

4 Conclusions and Future Work

Most post-fire processes are driven by water flow in an ecosystem (Martin, 2016), hence, a deeper understanding of how fires impact water flow is crucial. The present research highlights the implementation of a high-resolution, fully distributed, integrated hydrologic model designed to assess hydrologic alterations precipitated by wildfires in the Pacific Northwest. The four wildfires investigated in this study each display unique characteristics in terms of burn severity statistics and spatial distributions. The climatic regimes and landscape cover types of the watersheds influenced by these fires are presentative in the Pacific Northwest. The impact of SWR induced by the fires within their respective fire perimeters was incorporated into the model and found to significantly influence watershed hydrologic functions.

Modeling results reveal the LAI reduction caused by fire directly resulted in a decrease of simulated ET within the American River Watershed. This reduction can persist for years post-fire, gradually reverting to pre-fire dynamics with the recovery of the LAI. In a hypothetical scenario devoid of fire-induced LAI reduction, no significant changes in ET were observed.

An augmentation of 21-34% in post-fire peak flows were seen from the modeling results in the McKenzie River Watershed, the American River Watershed, and the Naches River Watershed as a result of the SWR effect triggered by fire. The Wenas Creek Watershed, conversely, only witnessed a 2% surge in post-fire peak flow, as a result of the Evans Canyon Fire's low burn severity. The Norse Peak Fire resulted in a mean reduction of 38% in the infiltration rate within the American River Watershed during the post-fire wet season. Additionally, post-fire peak flows in the McKenzie River Watershed and the Naches River Watershed escalated by 1-34% due to the SWR effect.

In a specific fire impacted watershed, a low post-fire precipitation rate inflicts minimal hydrologic disturbance, whereas a higher post-fire precipitation rate culminates in significant post-fire peak flows. This finding indicates that fire-induced watershed hydrology alterations are exacerbated by increased post-fire precipitation rates. However, as a consequence of the low burn severity of the Evans Canyon Fire, even a threefold increase in the post-fire precipitation rate did not yield significant differences in hydrologic response when comparing scenarios with and without the fire-induced SWR effect in the Wenas Creek Watershed. Moreover, for the same fire, the reduction in the Manning's coefficient due to vegetation loss attributable to the fire was observed to be more reactive to increasing post-fire peak flows, with a rise of 5-19% witnessed during various post-fire precipitation events.

Future work includes coupling ATS (integrated hydrology model) with PFLOTRAN (reactive transport model) (Hammond et al., 2014) and the PFLOTRAN sandbox (Hammond, 2022) to investigate the biogeochemistry of fire-affected watersheds. The model coupling

can be done through the Alquimia interface library (Andre et al., 2013). The coupled ATS-PFLOTRAN model (Molins et al., 2022; Xu et al., 2022) offers a robust framework for determining high-resolution biogeochemical spatial hot spots and key temporal moments in carbon and nitrogen cycling, in addition to identifying the fates of pyrogenic nutrients in fire-impacted watersheds.

Open Research

The source codes of the Advanced Terrestrial Simulator (ATS) model are available under the Berkeley Software Distribution (BSD) License at `https://github.com/amanzi/ats`. Publicly available data used in this study and their sources are summarized in Table A1 in Appendix A. Other input/output data from the model and the scripts to produce the figures of the manuscript are available at `https://data.ess-dive.lbl.gov/datasets/doi:10.15485/2006549` (Li et al., 2023). Figures were made with Python 3.10 (`https://www.python.org/`), Matplotlib version 3.5.1 (`https://matplotlib.org/`), and Paraview version 5.10.1 (`https://www.paraview.org/`). The study site map was made with ArcGIS Pro version 3.1.2 (`https://www.esri.com/en-us/arcgis/products/arcgis-pro/overview`).

Acknowledgments

This research was supported by the U.S. Department of Energy (DOE), Office of Science (SC) Biological and Environmental Research (BER) program, as part of BER's Environmental System Science (ESS) program. This research originates from the River Corridor Scientific Focus Area (SFA) at Pacific Northwest National Laboratory (PNNL) and the IDEAS-Watersheds project (funded by DOE, SC, BER program). PNNL is operated for DOE by Battelle Memorial Institute under contract DE-ACO5-76RL01830. This research used resources of the National Energy Research Scientific Computing Center (NERSC), which is supported by the DOE SC under contract DE-AC02-05CH11231. This paper describes objective technical results and analysis. Any subjective views or opinions that might be expressed in the paper do not necessarily represent the views of DOE or the United States government.

Appendix A. List of publicly available data used in this study as model inputs and for model performance evaluation

Table A1. Data sources and references

Inputs	Sources (Data managing agencies*)	References
	Vector data	
Watershed boundary	NHDPlus HR (USGS)	U.S. Geological Survey (2023b)
Stream network	NHDPlus HR (USGS)	U.S. Geological Survey (2023b)
Fire perimeter	MTBS (USDA, USGS)	Eidenshink et al. (2007)
	Static raster data	
DEM	3DEP (USGS)	U.S. Geological Survey (2023a)
Land cover	NLCD (USGS)	U.S. Geological Survey (2019)
Soil properties	SSURGO (USDA)	USDA Soil Survey Staff (2023)
Geology properties	GLHYMPS (Borealis)	Gleeson et al. (2014)
Soil thickness	SoilGrids (ISRIC)	Poggio et al. (2021)
Depth to bedrock	SoilGrids (ISRIC)	Poggio et al. (2021)
Burn severity	MTBS (USDA, USGS)	Eidenshink et al. (2007)
	Dynamic raster data	
Meteorological forcing	Daymet (ORNL)	Thornton et al. (2022)
Leaf area index	MODIS (NASA)	Myneni et al. (2015)
	Model evaluation data	
Streamflow discharge	NWIS (USGS)	U.S. Geological Survey (2023c)
Evapotranspirition	MODIS (NASA)	Running et al. (2017)

*USGS: U.S. Geological Survey;
USDA: U.S. Department of Agriculture;
Borealis: Canadian Dataverse Repository;
ISRIC: International Soil Reference and Information Centre;
ORNL: Oak Ridge National Laboratory;
NASA: National Aeronautics and Space Administration.

Appendix B. List of highest daily rainfall in the study watersheds

Table B1. High rainfall events in the wet seasons in 1980–2021

Year with High Rainfall Event in Wet Season	Daily Total Rainfall [mm]	Year with High Rainfall Event in Wet Season	Daily Total Rainfall [mm]
Mckenzie River		American River	
1996	110 (P_1)	2006	122 (P_1)
1999	72 (P_2)	2008	94 (P_2)
2012	64 (P_3)	2017	81 (P_3)
1998	62 (P_4)	1990	77 (P_4)
1994	57 (P_5)	2015	71 (P_5)
2013	55 (P_6)	1994	63 (P_6)
1984	50 (P_7)	2013	62 (P_7)
2006	49 (P_8)	1999	60 (P_8)
2016	48 (P_9)	1997	58 (P_9)
2017	46 (P_{10})	2012	57 (P_{10})
Naches River		Wenas Creek	
2006	91 (P_1)	2006	53 (P_1)
2008	68 (P_2)	2017	42 (P_2)
2017	62 (P_3)	1994	38 (P_3)
1990	57 (P_4)	1997	37 (P_4)
1997	52 (P_5)	2008	36 (P_5)
2015	50 (P_6)	1980	35 (P_6)
1994	48 (P_7)	1990	34 (P_7)
1980	46 (P_8)	2021	31 (P_8)
1999	45 (P_9)	2015	28 (P_9)
2021	43 (P_{10})	2016	25 (P_{10})

References

Abatzoglou, J. T., Battisti, D. S., Williams, A. P., Hansen, W. D., Harvey, B. J., & Kolden, C. A. (2021). Projected increases in western us forest fire despite growing fuel constraints. *Communications Earth & Environment*, *2*(1), 227.

Abatzoglou, J. T., Rupp, D. E., O'Neill, L. W., & Sadegh, M. (2021). Compound extremes drive the western oregon wildfires of september 2020. *Geophysical Research Letters*, *48*(8), e2021GL092520.

Agbeshie, A. A., Abugre, S., Atta-Darkwa, T., & Awuah, R. (2022). A review of the effects of forest fire on soil properties. *Journal of Forestry Research*, *33*(5), 1419–1441.

Andre, B., Molins, S., Johnson, J., & Steefel, C. (2013, aug). *Alquimia.* [Computer Software] `https://doi.org/10.11578/dc.20210416.49`. Retrieved from `https://doi.org/10.11578/dc.20210416.49` doi: 10.11578/dc.20210416.49

Bhanja, S. N., Coon, E. T., Lu, D., & Painter, S. L. (2023). Evaluation of distributed process-based hydrologic model performance using only a priori information to define model inputs. *Journal of Hydrology*, *618*, 129176.

Carrà, B. G., Bombino, G., Denisi, P., Plaza-Àlvarez, P. A., Lucas-Borja, M. E., & Zema, D. A. (2021). Water infiltration after prescribed fire and soil mulching with fern in mediterranean forests. *Hydrology*, *8*(3), 95.

Chen, L., Berli, M., & Chief, K. (2013). Examining modeling approaches for the rainfall-runoff process in wildfire-affected watersheds: Using san dimas experimental forest. *JAWRA Journal of the American Water Resources Association*, *49*(4), 851–866.

Coon, E. T., Moulton, J. D., Kikinzon, E., Berndt, M., Manzini, G., Garimella, R., ... Painter, S. L. (2020). Coupling surface flow and subsurface flow in complex soil structures using mimetic finite differences. *Advances in Water Resources*, *144*, 103701.

Coon, E. T., & Shuai, P. (2022). Watershed workflow: A toolset for parameterizing data-intensive, integrated hydrologic models. *Environmental Modelling & Software*, *157*, 105502.

Coon, E. T., Svyatsky, D., Jan, A., Kikinzon, E., Berndt, M., Atchley, A., ... Molins, S. (2019). *Advanced Terrestrial Simulator.* Retrieved from `https://doi.org/10.11578/dc.20190911.1` doi: 10.11578/dc.20190911.1

Cydzik, K., & Hogue, T. S. (2009). Modeling postfire response and recovery using the hydrologic engineering center hydrologic modeling system (hec-hms) 1. *JAWRA Journal of the American Water Resources Association*, *45*(3), 702–714.

DeBano, L. F. (2000a). The role of fire and soil heating on water repellency in wildland environments: a review. *Journal of hydrology*, *231*, 195–206.

DeBano, L. F. (2000b). Water repellency in soils: a historical overview. *Journal of hydrology*, *231*, 4–32.

DiBiase, R. A., & Lamb, M. P. (2020). Dry sediment loading of headwater channels fuels post-wildfire debris flows in bedrock landscapes. *Geology*, *48*(2), 189–193.

Ebel, B. A., & Moody, J. A. (2017). Synthesis of soil-hydraulic properties and infiltration timescales in wildfire-affected soils. *Hydrological Processes*, *31*(2), 324–340.

Ebel, B. A., Moody, J. A., & Martin, D. A. (2012). Hydrologic conditions controlling runoff generation immediately after wildfire. *Water Resources Research*, *48*(3).

Ebel, B. A., Rengers, F. K., & Tucker, G. E. (2016). Observed and simulated hydrologic response for a first-order catchment during extreme rainfall 3 years after wildfire disturbance. *Water Resources Research*, *52*(12), 9367–9389.

Ebel, B. A., Shephard, Z. M., Walvoord, M. A., Murphy, S. F., Partridge, T. F., & Perkins, K. S. (2023). Modeling post-wildfire hydrologic response: Review and future directions for applications of physically based distributed simulation. *Earth's Future*, *11*(2), e2022EF003038.

Eidenshink, J., Schwind, B., Brewer, K., Zhu, Z.-L., Quayle, B., & Howard, S. (2007). A project for monitoring trends in burn severity. *Fire ecology*, *3*(1), 3–21.

Garcia-Chevesich, P., Pizarro, R., Stropki, C., Ramirez de Arellano, P., Ffolliott, P., DeBano, L. F., ... Slack, D. (2010). Formation of post-fire water-repellent layers in monterrey pine (pinus radiata d. don) plantations in south-central chile. *Journal of soil science and plant nutrition*, *10*(4), 399–406.

Gleeson, T., Moosdorf, N., Hartmann, J., & Van Beek, L. (2014). A glimpse beneath earth's surface: Global hydrogeology maps (glhymps) of permeability and porosity. *Geophysical Research Letters*, *41*(11), 3891–3898.

Gupta, H. V., Kling, H., Yilmaz, K. K., & Martinez, G. F. (2009). Decomposition of the mean squared error and nse performance criteria: Implications for improving hydrological modelling. *Journal of hydrology*, *377*(1-2), 80–91.

Hallema, D. W., Sun, G., Caldwell, P. V., Norman, S. P., Cohen, E. C., Liu, Y., ... McNulty, S. G. (2018). Burned forests impact water supplies. *Nature communications*, *9*(1), 1307.

Hammond, G. E. (2022). The pflotran reaction sandbox. *Geoscientific Model Devel-*

opment, *15*(4), 1659–1676.

Hammond, G. E., Lichtner, P. C., & Mills, R. (2014). Evaluating the performance of parallel subsurface simulators: An illustrative example with pflotran. *Water resources research*, *50*(1), 208–228.

Kemter, M., Fischer, M., Luna, L., Schönfeldt, E., Vogel, J., Banerjee, A., ... Thonicke, K. (2021). Cascading hazards in the aftermath of australia's 2019/2020 black summer wildfires. *Earth's Future*, *9*(3), e2020EF001884.

Kinoshita, A. M., Hogue, T. S., & Napper, C. (2014). Evaluating pre-and post-fire peak discharge predictions across western us watersheds. *JAWRA Journal of the American Water Resources Association*, *50*(6), 1540–1557.

Kling, H., Fuchs, M., & Paulin, M. (2012). Runoff conditions in the upper danube basin under an ensemble of climate change scenarios. *Journal of hydrology*, *424*, 264–277.

Li, Z., Angerer, J. P., & Wu, X. B. (2021). Temporal patterns of large wildfires and their burn severity in rangelands of western united states. *Geophysical Research Letters*, *48*(7), e2020GL091636.

Li, Z., Li, B., Jiang, P., Hammond, G., Shuai, P., Zahura, F., ... Chen, X. (2023). Data and scripts associated with the manuscript evaluating the hydrologic responses of the pacific northwest watersheds to wildfires. *River Corridor and Watershed Biogeochemistry SFA, ESS-DIVE repository*. doi: 10.15485/2006549

Maina, F. Z., & Siirila-Woodburn, E. R. (2020). Watersheds dynamics following wildfires: Nonlinear feedbacks and implications on hydrologic responses. *Hydrological Processes*, *34*(1), 33–50.

Martin, D. A. (2016). At the nexus of fire, water and society. *Philosophical Transactions of the Royal Society B: Biological Sciences*, *371*(1696), 20150172.

Merz, R., Parajka, J., & Blöschl, G. (2009). Scale effects in conceptual hydrological modeling. *Water resources research*, *45*(9).

Moisseeva, N., & Stull, R. (2021). Wildfire smoke-plume rise: a simple energy balance parameterization. *Atmospheric Chemistry and Physics*, *21*(3), 1407–1425.

Molins, S., Svyatsky, D., Xu, Z., Coon, E. T., & Moulton, J. D. (2022). A multicomponent reactive transport model for integrated surface-subsurface hydrology problems. *Water Resources Research*, *58*(8), e2022WR032074.

Moody, J. A. (2012). *An analytical method for predicting postwildfire peak discharges*. US Department of the Interior, US Geological Survey.

Moody, J. A., & Ebel, B. A. (2012). Hyper-dry conditions provide new insights into the cause of extreme floods after wildfire. *Catena*, *93*, 58–63.

Moody, J. A., Ebel, B. A., Nyman, P., Martin, D. A., Stoof, C., & McKinley, R. (2015). Relations between soil hydraulic properties and burn severity. *International Journal of Wildland Fire*, *25*(3), 279–293.

Murphy, S. F., McCleskey, R. B., Martin, D. A., Writer, J. H., & Ebel, B. A. (2018). Fire, flood, and drought: extreme climate events alter flow paths and stream chemistry. *Journal of Geophysical Research: Biogeosciences*, *123*(8), 2513–2526.

Murphy, S. F., Writer, J. H., McCleskey, R. B., & Martin, D. A. (2015). The role of precipitation type, intensity, and spatial distribution in source water quality after wildfire. *Environmental Research Letters*, *10*(8), 084007.

Myneni, R., Knyazikhin, Y., & Park, T. (2015). Mod15a2h modis leaf area index/fpar 8-day l4 global 500m sin grid v006. nasa eosdis land processes daac. *LP DAAC, Terra*, *6*(1).

Nash, J. E., & Sutcliffe, J. V. (1970). River flow forecasting through conceptual models part i—a discussion of principles. *Journal of hydrology*, *10*(3), 282–290.

Oleson, K., Lawrence, D., Bonan, G., Drewniak, B., Huang, M., Koven, C., ... oth-

ers (2010). Technical description of version 4.5 of the community land model (clm), ncar tech. *Notes (NCAR/TN-478+ STR), 605*.

Parsons, A. (2003). Burned Area Emergency Rehabilitation (BAER) soil burn severity definitions and mapping guidelines. *USDA Forest Service, Rocky Mountain Research Station, Missoula*.

Parsons, A., Robichaud, P. R., Lewis, S. A., Napper, C., & Clark, J. T. (2010). *Field guide for mapping post-fire soil burn severity* (Vol. 243). Citeseer.

Paul, M., LeDuc, S., Lassiter, M., Moorhead, L., Noyes, P., & Leibowitz, S. (2022). Wildfire induces changes in receiving waters: A review with considerations for water quality management. *Water Resources Research*, *58*(9), e2021WR030699.

Poggio, L., de Sousa, L. M., Batjes, N. H., Heuvelink, G. B. M., Kempen, B., Ribeiro, E., & Rossiter, D. (2021). Soilgrids 2.0: producing soil information for the globe with quantified spatial uncertainty. *SOIL*, *7*(1), 217–240. Retrieved from `https://soil.copernicus.org/articles/7/217/2021/` doi: 10.5194/soil-7-217-2021

Rastogi, D., Kao, S.-C., & Ashfaq, M. (2022). How may the choice of downscaling techniques and meteorological reference observations affect future hydroclimate projections? *Earth's Future*, *10*(8), e2022EF002734.

Rengers, F. K., McGuire, L. A., Kean, J. W., Staley, D. M., & Hobley, D. (2016). Model simulations of flood and debris flow timing in steep catchments after wildfire. *Water Resources Research*, *52*(8), 6041–6061.

Robbins, W. G. (2021). Oregon and climate change: The age of megafires in the american west. *Oregon Historical Quarterly*, *122*(3), 250–277.

Robinne, F.-N., Hallema, D. W., Bladon, K. D., & Buttle, J. M. (2020). Wildfire impacts on hydrologic ecosystem services in north american high-latitude forests: A scoping review. *Journal of Hydrology*, *581*, 124360.

Robinne, F.-N., Hallema, D. W., Bladon, K. D., Flannigan, M. D., Boisramé, G., Bréthaut, C. M., ... others (2021). Scientists' warning on extreme wildfire risks to water supply. *Hydrological Processes*, *35*(5), e14086.

Roebuck Jr, J. A., Bladon, K. D., Donahue, D., Graham, E. B., Grieger, S., Morgenstern, K., ... others (2022). Spatiotemporal controls on the delivery of dissolved organic matter to streams following a wildfire. *Geophysical Research Letters*, *49*(16), e2022GL099535.

Roth, H. K., McKenna, A. M., Simpson, M. J., Chen, H., Srikanthan, N., Fegel, T. S., ... Borch, T. (2023). Effects of burn severity on organic nitrogen and carbon chemistry in high-elevation forest soils. *Soil & Environmental Health*, 100023.

Running, S., Mu, Q., & Zhao, M. (2017). Mod16a2 modis/terra net evapotranspiration 8-day l4 global 500m sin grid v006. *LP DAAC, Terra*.

Shewchuk, J. R. (2002). Delaunay refinement algorithms for triangular mesh generation. *Computational geometry*, *22*(1-3), 21–74.

Shuai, P., Chen, X., Mital, U., Coon, E. T., & Dwivedi, D. (2022). The effects of spatial and temporal resolution of gridded meteorological forcing on watershed hydrological responses. *Hydrology and Earth System Sciences*, *26*(8), 2245–2276.

Thornton, M., Shrestha, R., Wei, Y., Thornton, P., Kao, S.-C., & Wilson, B. (2022). *Daymet: Daily surface weather data on a 1-km grid for north america, version 4 r1.* ORNL Distributed Active Archive Center. Retrieved from `https://daac.ornl.gov/cgi-bin/dsviewer.pl?ds_id=2129` doi: 10.3334/ORNLDAAC/2129

U.S. Geological Survey. (2019). National Land Cover Database (NLCD) 2016 Land Cover Science Product).

U.S. Geological Survey. (2023a). 1 Arc-second Digital Elevation Models (DEMs) - USGS National Map 3DEP Downloadable Data Collection.

U.S. Geological Survey. (2023b). National Hydrography Dataset Plus High Resolution (NHDPlus HR).

U.S. Geological Survey. (2023c). National Water Information System data available on the World Wide Web (USGS Water Data for the Nation).

USDA Soil Survey Staff. (2023). Soil Survey Geographic (SSURGO) Database.

Vieira, D., Fernández, C., Vega, J., & Keizer, J. (2015). Does soil burn severity affect the post-fire runoff and interrill erosion response? a review based on meta-analysis of field rainfall simulation data. *Journal of Hydrology*, *523*, 452–464.

Wagenbrenner, J. W., Ebel, B. A., Bladon, K. D., & Kinoshita, A. M. (2021). Post-wildfire hydrologic recovery in mediterranean climates: A systematic review and case study to identify current knowledge and opportunities. *Journal of Hydrology*, *602*, 126772.

Wall, S., Roering, J., & Rengers, F. K. (2020). Runoff-initiated post-fire debris flow western cascades, oregon. *Landslides*, *17*, 1649–1661.

Wampler, K., Bladon, K., & Faramarzi, M. (2023). Modeling wildfire effects on streamflow in the cascade mountains, oregon, usa. *Journal of Hydrology*, *621*, 129585.

Wieting, C., Ebel, B. A., & Singha, K. (2017). Quantifying the effects of wildfire on changes in soil properties by surface burning of soils from the boulder creek critical zone observatory. *Journal of Hydrology: Regional Studies*, *13*, 43–57.

Wilder, B. A., Lancaster, J. T., Cafferata, P. H., Coe, D. B., Swanson, B. J., Lindsay, D. N., ... Kinoshita, A. M. (2021). An analytical solution for rapidly predicting post-fire peak streamflow for small watersheds in southern california. *Hydrological Processes*, *35*(1), e13976.

Wilmot, T. Y., Mallia, D. V., Hallar, A. G., & Lin, J. C. (2022). Wildfire plumes in the western us are reaching greater heights and injecting more aerosols aloft as wildfire activity intensifies. *Scientific reports*, *12*(1), 12400.

Wine, M. L., & Cadol, D. (2016). Hydrologic effects of large southwestern usa wildfires significantly increase regional water supply: fact or fiction? *Environmental Research Letters*, *11*(8), 085006.

Xu, Z., Molins, S., Özgen-Xian, I., Dwivedi, D., Svyatsky, D., Moulton, J. D., & Steefel, C. (2022). Understanding the hydrogeochemical response of a mountainous watershed using integrated surface-subsurface flow and reactive transport modeling. *Water Resources Research*, *58*(8), e2022WR032075.

Zema, D. A., Lucas-Borja, M. E., Fotia, L., Rosaci, D., Sarnè, G. M., & Zimbone, S. M. (2020). Predicting the hydrological response of a forest after wildfire and soil treatments using an artificial neural network. *Computers and electronics in agriculture*, *170*, 105280.